Geothermal Energy

RESEARCH Open Access

Experimental study on the effect of CO_2 storage on the reservoir permeability in a CO_2-based enhanced geothermal system

Pan Li[1,2*], Yang Hao[2], Yu Wu[2], Ayal Wanniarachchi[3], Hongxue Zhang[1] and Zhili Cui[1]

*Correspondence:
plee@cumt.edu.cn

[1] School of Mechanics and Optoelectronics Physics, Anhui University of Science and Technology, No. 168 Taifeng Road, Huainan 232001, Anhui, China
[2] State Key Laboratory for Geomechanics and Deep Underground Engineering, China University of Mining and Technology, Xuzhou 221116, Jiangsu, China
[3] Department of Civil Engineering, Monash University, Building 60, Melbourne, VIC 3800, Australia

Abstract

A CO_2-based Enhanced Geothermal System (CO_2-EGS) has dual benefits of heat extraction and CO_2 storage. Mineralization storage of CO_2 may reduce reservoir permeability, thereby affecting heat extraction. Solutions require further research to optimize and balance these two benefits. In this study, CO_2 storage and heat extraction were simulated by alternating cyclic injection of water and supercritical CO_2 into fractured granite. By analyzing the changes of ion composition in water samples and the minerals of fracture surface, the mechanisms controlling the fracture permeability with and without proppant were obtained. The results suggest that monticellite and vaterite were formed besides montmorillonite, calcite and illite after increasing the injection cycles. This promotes mineralization storage of CO_2 but reduces reservoir permeability. Without proppant, the permeability decreased in three stages and the reduction rate exhibited a sharp-slow–fast–slow trend. While the use of proppant caused an increase of two orders of magnitude in permeability. Therefore, increasing the non-contact area of the main fracture and the CO_2 flow velocity can avoid a large decrease in permeability, which will increase the heat extraction and mineralization storage of CO_2. The findings provide solutions for the CO_2 emission reduction and the efficient exploitation of hot dry rock.

Keywords: Enhanced geothermal system, CO_2 emission reduction, Permeability, Fractured granite

Introduction

The ever-increasing CO_2 emissions have a significant impact on climate change and lead to many extreme climate events, including floods, wildfires, and heat waves (Meinshausen et al. 2022; Guo et al. 2019). Therefore, many studies have focused on low-carbon production technology, CO_2 capture and storage technology, and how to achieve carbon emission reduction by government legislative intervention and market regulation (Subramanian et al. 2019; Frank et al. 2019; Deng et al. 2019; Ager and Lapkin 2018). Renewable energy is central to invigorating the transition to a low-carbon and sustainable energy system (IEA 2021). In the long term, renewable energy consumption per capita increases by 1%, the per capita carbon emissions will be reduced by 0.259% (Li

and Haneklaus 2021). As a renewable energy, hot dry rock (HDR) geothermal energy has huge reserves. Compared to the solar energy and wind energy, the exploitation of HDR is characterized by stability and seasonal independence (Hou et al. 2018; Liao et al. 2020). To increase the heat extraction and reduce the carbon emission, a novel solution has been proposed that using CO_2-based Enhanced Geothermal Systems (CO_2-EGSs) for HDR exploitation (Pruess 2006).

At present, how to improve the heat extraction rate is one of the main difficulties in HDR exploitation. The flow rate of CO_2 is significantly affected by reservoir permeability, which is a key factor affecting the heat extraction rate. Existing studies have shown that the permeability is influenced by the fracture aperture, fracture surface roughness, pressure and temperature of the heat extraction fluid, and the reservoir temperature (Shu et al. 2020; Guo et al. 2017; Kamali-Asl et al. 2018). Accordingly, a series of solutions have been proposed to improve reservoir permeability. Such as the use of proppant and the reservoir stimulation by microwave heating. The former is a common strategy for increasing the fracture aperture, but a high seepage pressure can redistribute the proppant's action range and reduce the propping effectiveness (Huang et al. 2021). Fracture permeability is very sensitive to the rock mass's temperature (Song et al. 2021). When granite is heated above 600 °C, its permeability can increase by about two orders of magnitude (Liu et al. 2020). Therefore, reservoir stimulation by microwave heating may be an effective method. In addition, it is necessary to evaluate the enhancement effects of permeability under different methods. It has been found that permeability is independent of the average aperture and fracture size within a specific contact area. Moreover, the permeability can be predicted based on the change in the resistivity ratio between the saturated rock and the fluid (Sawayama et al. 2021).

The injection of CO_2 may result in CO_2-water–rock interactions, which have a significant impact on the reservoir permeability. In the EGS reservoir with granite-dominated rock, the hydrothermal alteration of granite causes the dissolution of primary minerals and the crystallization of newly formed phases on fracture surfaces, which can improve the porosity. While the crystallization of illite and calcite decreases the permeability (Ledésert et al. 2010). In the two possible types of granite alteration, vein alteration can form carbonate, quartz and some clay minerals, which significantly change the granite overall porosity. And these processes are greatly influenced by the reservoir temperature and the chemical characteristics of fluid. In addition, chemical dissolution and mechanical creep of the protrusions on the fracture surfaces will reduce the aperture and permeability (Caulk et al. 2016). However, long-term CO_2-water–rock interactions may cause silicification and embrittlement of granite, which results in the extension of shear failure and the increase of permeability (Dempsey et al. 2015). Through numerical analysis, we found that the permeability is relatively less sensitive to mechanical and hydraulic effects, and the thermal effect has short- or medium-term influences on the permeability, while the chemical effect has long-term and significant influences on the permeability (Tao et al. 2019).

Several experimental studies have been conducted to analyze CO_2-water–rock interactions by placing block or powdered samples in a reaction kettle containing CO_2 solution (Na et al. 2015; Liu et al. 2003; Ueda et al. 2005; Ré et al. 2014). In addition, by injecting a mixture of CO_2 and water, one study analyzed the effect of this method on the

production sustainability of a two-phase geothermal reservoir (Kaya et al. 2018). However, for the influences of chemical effect on the permeability of CO_2-EGS reservoirs, few studies have comprehensively considered the two-phase flow of CO_2 and water coupled Thermo-Hydro-Mechanical-Chemical (THMC) effect. In this regard, based on our previous research (Wu and Li 2020; Wu et al. 2021), a novel experimental method of alternating cyclic injection of water and supercritical CO_2 (CO_2 (sc)) into fractured granite was adopted in this study. By increasing the number of injection cycles, the influences of the coupled THMC effect on the fracture surfaces' morphology and mineral crystallization were studied, and the mechanisms controlling the fracture permeability with and without proppant were obtained. The results of this study provide technical support for increasing the heat extraction rate of the CO_2-EGS and the CO_2 emission reduction.

Materials and methods

Experimental installation

A schematic diagram of the triaxial seepage system used in this study to produce the coupled THMC effect is shown in Fig. 1. The experimental system consists of four units, including the CO_2 (sc) preparation unit (*Unit I*), the water injection/pressurization unit (*Unit II*), the high-temperature seepage unit (*Unit III*) and the system control and data acquisition unit (*Unit IV*). In the preparation of CO_2 (sc), the CO_2 cylinder is connected to the booster pump, the air compressor and the booster pump are opened to pressurize CO_2, and the pressurized CO_2 is stored in the high pressure gasholder. Then, the preheater is opened to inject the CO_2. The pressure regulating valve is used to adjust the injection pressure, and the inlet pressure sensor of *Unit II* is observed to reach the set value. The pressure is maintained for continuous injection for 1 h, until the temperature of CO_2 flowing through the preheater does not exceed 0.5 °C, then CO_2 reaches the supercritical state. During the experiment, pressures are exerted on the rock sample by the axial pressure pump and the confining pressure pump in unit II. Water is injected through the water injection pump, and the injection water is measured in real time. The

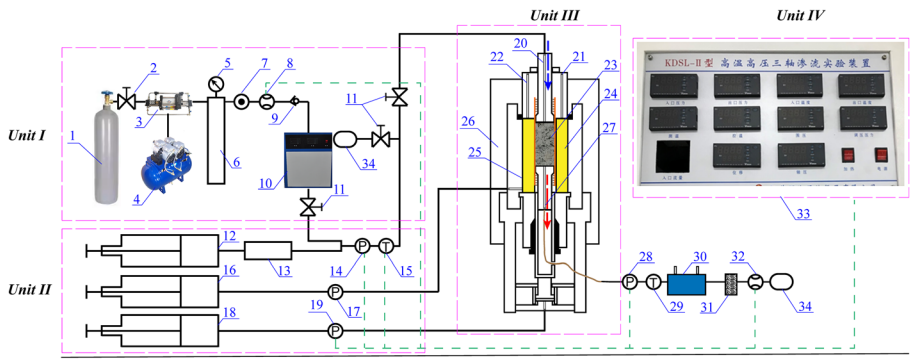

1-Gas source **2(11)**-Stop valves **3**-Booster pump **4**- Air compressor **5**-Pressure gage
6-High pressure gasholder **7**-Pressure regulating valve **8**-Inlet flowmeter **9**-Non-return valve
10-Preheater **12**-Water injection pump **13**-Displacement meter **14**-Inlet pressure sensor
15-Inlet temperature sensor **16**-Confining pressure pump **17**-Confining pressure sensor **18**-Axial pressure pump
19-Axial pressure sensor **20**-Cold fluid inlet **21**-Temperature measurement channel **22**-Air exhaust channel
23-Core of rock **24**-Oil chamber **25**-Electric heating device **26**-Thermal insulation device
27-Hot fluid outlet **28**-Outlet pressure sensor **29**-Outlet temperature sensor **30**-Condenser
31-Gas dryer **32**-Outlet flowmeter **33**-Data collection system **34**-Lye pool

Fig. 1 Schematic diagram of the triaxial seepage experimental system for producing the coupled thermo-hydro-mechanical-chemical effect

pressure sensors and temperature sensors are used to collect the pressures and temperatures of CO_2 at injection port and flow outlet, respectively. The temperature control probe and the temperature measuring probe in the triaxial seepage chamber are used to measure the heating temperature and the rock sample temperature, respectively. Finally, all the pressures and temperatures during the experiment are collected and stored in real time through the data collection system.

The hydro effect is realized by the *Unit I*, *Unit II*, and *Unit III*. *Unit I* can prepare CO_2 (sc) with a pressure of 7.5–20 MPa and a temperature of 40–100 °C. The thermo and chemical effects are achieved primarily using *Unit III*, in which the granite can be heated to a maximum temperature of approximately 300 °C using a high-temperature oil bath. Therefore, CO_2-water–rock interactions may occur on the surfaces of the fractures in the granite. The fracture water sample during each injection cycle can be collected using *Unit IV* to analyze its ionic composition and content. The mechanical effect is realized using *Unit II* and *Unit III*. The axial pressure pump and confining pressure pump in *Unit II* supply the triaxial pressure on the rock sample, and the pressure provided by both units can reach 60 MPa.

Experimental design and rock sample preparation

Two groups of experiments were designed in this study, including heat extraction experiments with and without proppant in the fractures. The granite used in this experiment was from the high heat flow granite in Zhangzhou, Fujian Province of China, and the fractured granite samples were prepared using the Brazilian splitting method (Shams et al. 2023). Since the first group of experiments was perfected based on our previous carbon storage studies, the rock samples and experimental conditions were consistent with those used in our previous study (Wu et al. 2021). Figure 2 shows the first group of experimental rock samples with a diameter and height of 50 mm, namely, fractured granite samples CA-1 and CA-2 without proppant.

In the first group of experiments, to analyze the influence of the number of alternating injection cycles on the permeability, rock samples CA-1 and CA-2 were subjected to six and nine injection cycles, respectively, and each cycle lasted for 3 days. In this study, using the condition of hot dry rock at Bad Urach in Germany as the background, the rock samples were subjected to a confining pressure of 30 MPa and an axial pressure of 35 MPa. The rock samples were heated to 200 °C (simulated reservoir

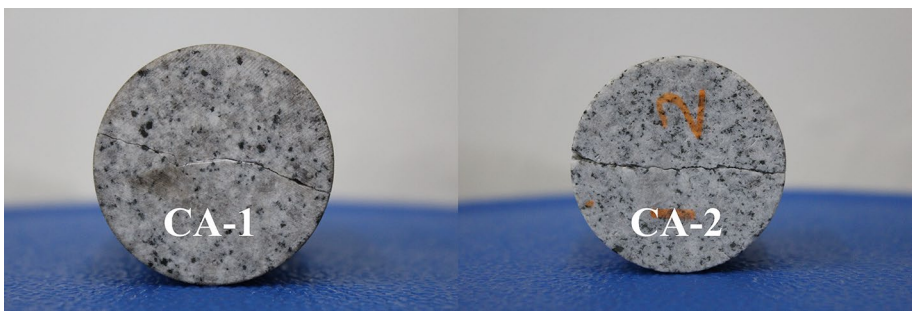

Fig. 2 Fractured granite samples CA-1 and CA-2 without proppant

Fig. 3 Fracture water samples collected during each injection cycle for rock sample CA-2 and pH testing

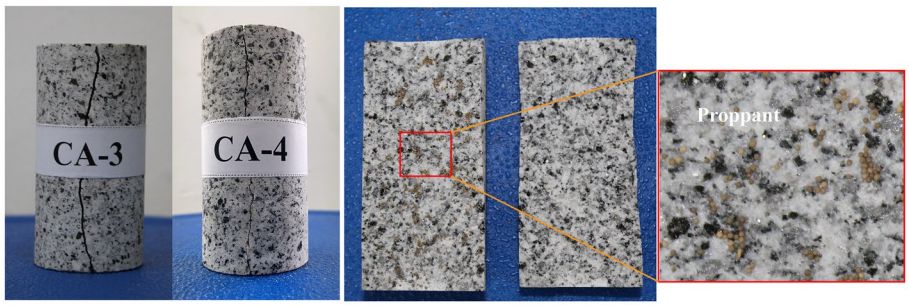

Fig. 4 Fractured granite samples CA-3 and CA-4 with proppant

temperature), and the CO_2 injection pressure and temperature were 7.5 MPa and 40 °C [i.e., CO_2 (sc)], respectively. Similar to the experimental method for the rock sample CA-1, we collected fracture water samples from rock sample CA-2 during each injection cycle and analyzed the ion compositions and contents. Figure 3 shows the fracture water samples collected during each injection cycle and the pH testing process.

Figure 4 shows fractured granite samples CA-3 and CA-4 with proppant. The proppant was sintered from high-quality bauxite and was 300–600 μm in size. In addition, it has the advantages of a high strength (> 52 MPa), a wear resistance at high temperatures, and is insoluble in water. The proppant was added in a different way than in a real reservoir. First, the proppant was spread evenly over the fracture surfaces in half of the rock sample. This part of the rock sample was then fitted to the other part. Finally, high temperature resistant (~ 260 °C) Teflon seal tape was wrapped tightly around the rock sample to prevent the proppant from falling off. The rock sample was then placed in the core holder of *Unit III*.

Using the first group as the control experiments, the second group of experiments was designed to explore whether the mineral dissolution or that of the mineral precipitation affected the fracture permeability more under CO_2-water–rock interactions. Therefore, in the two groups of experiments, the same CO_2 (sc) injection conditions, pressure and temperature were applied to the rock sample. To increase the zone affected by the proppant, the heights of rock samples CA-3 and CA-4 were double the height (i.e., 100 mm) of the rock samples in the first group.

Fracture permeability calculation

A permeability test of a gas with a high compressibility in a rock sample needs to consider two aspects. One is the possible gas slip phenomenon (Klinkenberg effect) under a lower average flow pressure, and the other is the inertia effect of high-speed flow (Caulk et al. 2016). CO_2 (sc) with a high flow pressure was used as the working fluid in the experiments, so the Klinkenberg effect could be ignored. The Reynolds number (*Re*) of the fluid flow has been widely used to evaluate the influence of the inertia effect in flow systems, so it was necessary to first estimate the Reynolds number of the CO_2 (sc) flow in the fractured granite. In the experiments, the rock sample was a cylindrical fractured granite sample with a diameter of 50 mm and a height of 50 mm (or 100 mm). According to the definition of the fluid flow state in hydraulics, the Reynolds number of the CO_2 (sc) flow in the fracture was calculated as follows (Kolditz 2001):

$$Re = \frac{2v_f w \rho_f}{\mu} \tag{1}$$

where v_f is the average flow velocity of the CO_2, w is the average fracture aperture, ρ_f is the density of the CO_2, and μ is the dynamic viscosity of the CO_2.

In this study, the maximum average fracture aperture in the two groups of experimental rock samples was about 0.318 mm. Owing to the effect of the confining pressure, the fracture aperture was less than this value. Other parameters such as the average velocity v_f and density ρ_f of the CO_2 (sc) were taken as the maximum values, and the dynamic viscosity μ was taken as the minimum value. Using Eq. (1), the maximum Reynolds number was estimated to be 3.8.

When $Re > 1$, the fluid flow exhibits the characteristics of non-Darcy flow. However, when $1 < Re < 10$, the inertial force producing the nonlinear effect in the fracture flow is very weak (Ranjith and Viete 2011). Therefore, the influence of the inertial force on the flow could be ignored in this study, and it is believed that the process of the CO_2 (sc) flow in the fractured granite satisfied Darcy's law. Thus, the permeability of the fracture can be obtained as follows (Caulk et al. 2016):

$$k = \frac{b^2 \rho_f g}{12} \tag{2}$$

$$\frac{p_{in}^2 - p_{out}^2}{2 p_{out} L} = \frac{12 \mu Q_f}{b^3 w \rho_f g} \tag{3}$$

where k is the permeability, b is the equivalent hydraulic aperture, g is the acceleration due to gravity, p_{in} and p_{out} are the pressures of the CO_2 at the inlet and outlet, respectively, L is the length of the rock sample, and Q_f is the volume flow rate of the CO_2.

Results and discussion

Chemical properties of water in fractures

The chemical properties of the water samples from rock sample CA-1 can refer to our previous study (Wu and Li 2020). From the initial stage to the 6th injection cycle, the pH of the water sample was reduced from 6.5 to 4.7. For other ions, the concentrations of Cl^-, NO_3^- and SO_4^{2-} did not change significantly in each injection cycle. The Na^+ concentration increased from 4.7 mg/L to 26.9 mg/L, and K^+ concentration increased from 5.2 mg/L to 106.1 mg/L, and then decreased to 24.9 mg/L. The Ca^{2+} concentration fluctuated continuously during the six injection cycles, indicating that Ca-containing minerals dissolved and precipitated. The Mg^{2+} concentration increased slowly from 1.4 mg/L to 4.1 mg/L. Figure 5 shows the changes in the pH of the fracture water samples from rock sample CA-2 during each injection cycle. Similar to rock sample CA-1, after the first injection cycle, the pH changed from approximately neutral to slightly acidic. Then, as the number of injection cycles increased, the pH cyclically increased and decreased slightly. This indicates that the continuous dissolution of a small amount of CO_2 caused the dissolution and precipitation of minerals on the fracture surfaces, which led to the constant generation and consumption of H^+. The specific forms of mineral dissolution and precipitation were preliminarily identified based on the changes in the ion compositions and contents of the water samples.

The changes in the ion composition and content of the water samples from rock sample CA-2 are shown in Fig. 6. It can be seen that during injection cycles 0–2, the Mg^{2+} content did not change significantly, while the Na^+ and Ca^{2+} contents increased slowly, and the K^+ content decreased significantly. This indicates that the decrease in the pH caused the dissolution of feldspars such as albite and anorthite, releasing the corresponding cations into the fracture water, generating illite precipitation under the K-rich

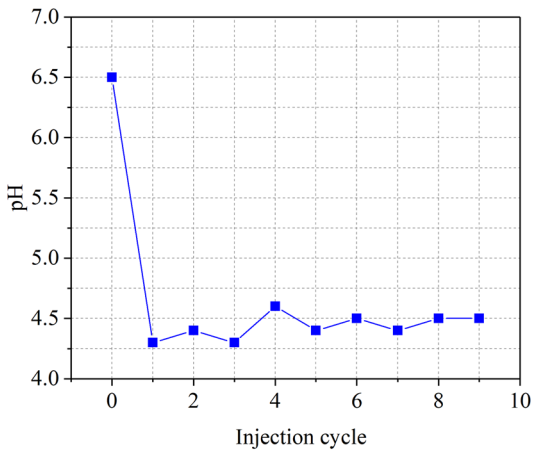

Fig. 5 Changes in the pH of the fracture water samples from rock sample CA-2 during each injection cycle

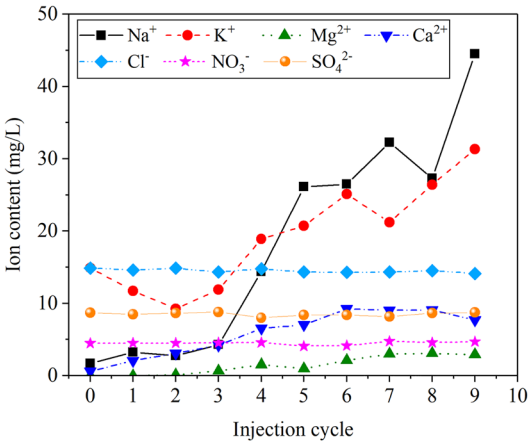

Fig. 6 Changes in the ion content of the water samples from rock sample CA-2

conditions, and reducing the K^+ content. The following geochemical reactions may be present in the above processes.

$$2\,\text{potassium feldspar} + 2H^+ + 9H_2O \rightarrow 2K^+ + \text{kaolinite} + 4H_4SiO_4 \tag{4}$$

$$3\,\text{albite} + K^+ + 2H^+ \rightarrow \text{illite} + 3Na^+ + 6SiO_6 \tag{5}$$

$$3\,\text{anorthite} + 2K^+ + 4H^+ \rightarrow \text{illite} + 3Ca^{2+} \tag{6}$$

During injection cycles 2–5, the Mg^{2+} content increased slightly, and the rate of increase of the K^+ content exhibited a slow–fast–slow trend, indicating that the biotite dissolved as the Na^+ and Ca^{2+} contents increased, and small amounts of Mg^{2+} and K^+ were generated. The rapid increase in the K^+ content indicates that the dissolution of potassium feldspar may also have occurred. The rate of increase of the Na^+ content gradually increased, while that of the Ca^{2+} content gradually decreased. It shows that calcite, illite, and kaolinite may have precipitated as the potassium feldspar, albite, and calcium feldspar dissolved. In addition, the Mg^{2+} content initially increased and then decreased gradually, which indicates that dolomite precipitation (containing Ca/Mg) also occurred. Relevant geochemical reactions may include:

$$\text{biotite} + 3Al^{3+} + Si^{4+} + 6H_2O \rightarrow K^+ + Al_4Si_4O_{10}(OH)_8 + 3Fe^{2+} + 3Mg^{2+} + 6H^+ + 2F^- \tag{7}$$

$$\text{anorthite} + H^+ + HCO_3^- + H_2O \rightarrow \text{kaolinite} + \text{calcite} \tag{8}$$

$$2\,\text{albite} + 2H^+ + 9H_2O \rightarrow \text{kaolinite} + 2Na^+ + 4H_4SiO_4 \tag{9}$$

$$2\,\text{potassium feldspar} + 2H^+ + 9H_2O \rightarrow 2K^+ + \text{kaolinite} + 4H_4SiO_4 \tag{10}$$

$$3\,\text{anorthite} + 2K^+ + 4H^+ \rightarrow \text{illite} + 3Ca^{2+} \tag{11}$$

$$\begin{aligned} &2\,\text{plagioclase} + 1.5\,\text{potassium feldspar} + 0.8\,Mg^{2+} \\ &+ 0.25\,Fe^{2+} + 2.2CO_2 + 4H_2O + \rightleftharpoons 1.4Na^+ \\ &+ 0.8K^+ + HCO_3^- + \text{kaolinite} + \text{illite} - \text{montmorillonite} \\ &+ 4.4\,\text{quartz} + 6\,\text{dolmite} \end{aligned} \tag{12}$$

During injection cycles 5–6, the contents of the four cations increased at different rates. The rate of increase of the Na^+ content was slow, while that of the other three cations were fast. This demonstrates that the precipitation of calcite, illite, and dolomite consumed the Ca^{2+}, K^+, and Mg^{2+} in the fracture water, respectively, and promoted the dissolution of anorthite and potassium feldspar. Furthermore, owing to the high Na^+ and K^+ contents, the dissolution of biotite was promoted. The dissolution of these minerals increased the rates of increase of the Ca^{2+}, K^+, and Mg^{2+} contents, but decreased the rate of increase of the Na^+ content, indicating that the precipitation of Na containing cancrinite may have occurred. The possible geochemical reactions involved include Formulas (7), (8), (10), (11) and (12).

During injection cycles 6–8, the Mg^{2+} and Ca^{2+} contents gradually stabilized, indicating that the precipitation consumption and dissolution generation of Mg^{2+} and Ca^{2+} became balanced. Nevertheless, the K^+ content decreased as the Na^+ content increased, indicating that the K-rich solution promoted the dissolution of albite and generated illite. The consumption of K^+ promoted the dissolution of potassium feldspar and released K^+ into the fracture water. In addition, the precipitation of cancrinite consumed Na^+ and reduced its content. The possible geochemical reactions involved include Formulas (5) and (10).

During injection cycles 8–9, the Na^+ and K^+ contents continued to increase, while the Mg^{2+} content did not change significantly, and the Ca^{2+} content slightly decreased. This indicates that only calcite was generated. The dissolution of albite did not consume K^+, and the kaolinite was precipitated during this process. The possible geochemical reactions involved include Formulas (8), (9) and (10).

Analysis of mineral changes on the fracture surfaces

The analysis of X-Ray Diffraction (XRD) and the observations of Scanning Electron Microscopy (SEM) revealed the compositions of the minerals on the fracture surfaces of rock sample CA-1, which were described in our previous study (Wu et al. 2021). The mineral compositions on the fracture surfaces of rock sample CA-2 obtained by XRD are shown in Fig. 7. Since rock samples CA-1 and CA-2 were prepared from two parts of a standard rock sample, the two samples had the same primary mineral composition (Fig. 7a). Compared to injection cycle 0, new minerals were formed after injection cycle 9, including cancrinite, vaterite (a thermally unstable phase of $CaCO_3$), dolomite, kaolinite, illite, and monticellite (silicate minerals containing Ca and Mg) (Fig. 7b).

The results are generally consistent with the analysis of changes in the ion contents of the water samples presented in Sect. "Chemical properties of water in fractures". The difference is that monticellite is present in the XRD analysis results. Therefore, the rates

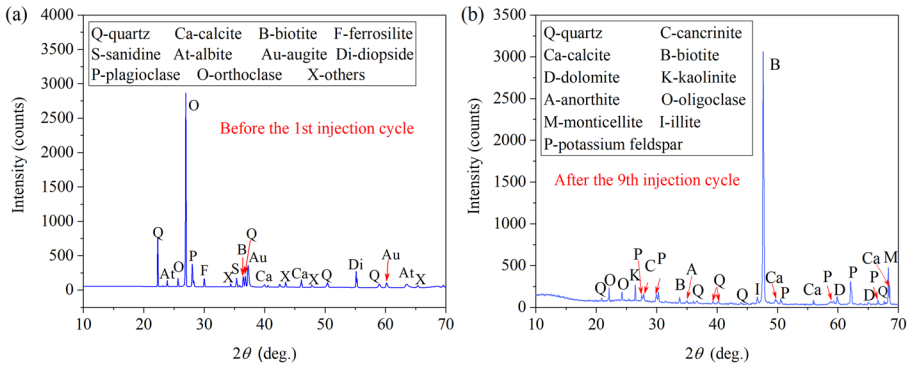

Fig. 7 XRD analysis of mineral compositions on fracture surfaces of rock sample CA-2. **a** is before the 1st injection cycle (Wu et al. 2021), **b** is after the 9th injection cycle

of increase of the Ca^{2+} and Mg^{2+} contents of the water samples slowed down or even slightly decreased, which indicates the formation of monticellite. The specific minerals were further qualitatively analyzed using SEM.

After injection cycle 9, blocky samples were collected from the fracture surface in rock sample CA-2 and three areas were selected for SEM combined Energy Dispersive Spectroscopy (SEM–EDS) analysis of the surface minerals. In area 1 (Fig. 8), Mg, Al, K, and Si are the minor elements at points 1–1 and 1–2 (generally Wt % $\leq$ 5% can be regarded as minor elements, and Wt% $\leq$ 0.5% can be regarded as trace elements). Therefore, the minerals at the above two points were identified as calcite according to their compositions. The difference is that the calcite at point 1–1 is the mineral base (i.e., the primary mineral) on the fracture surface, while the calcite at point 1–2 is a small granular mineral crystallization, which is obviously a new mineral formed via chemical reactions. Therefore, the Ca^{2+} at and around point 1–2 may have been derived from the dissolution of primary calcite or anorthite.

At point 1–3, first, the morphology shows that it is the mineral base of the fracture, which has many dissolution pores on the surface, so it may be a feldspar mineral. Then, according to the element composition, without considering the trace element K, the atomic number ratio of the other elements was calculated to be O:Ca:Si:Al:C:Na = 15.8:2.2:4.8:3:4:1. It can be concluded that the mineral is mainly oligoclase, and there may be few calcite crystals.

At point 1–4, the mineral occurrence is rod-like crystal clusters, indicating that it is a new mineral formed in the experiment. Without considering the trace elements and based on the contents of the different elements present, it can be identified as the thermally stable calcite phase of $CaCO_3$.

The SEM–EDS analysis results of the mineral components in area 2 are shown in Fig. 9. At point 2–1, the mineral base of the fracture surface is the same as that at point 1–3. The mineral has obvious dissolution pores and occurs as highly crystalline rods with granular mineral particles around them. In addition, the atomic number ratio of each element is O:Ca:Si:Al:C:Na = 17.25:3.6:2.6:2.96:4.57:1, so it is concluded to be oligoclase with a small amount of calcite crystal grains.

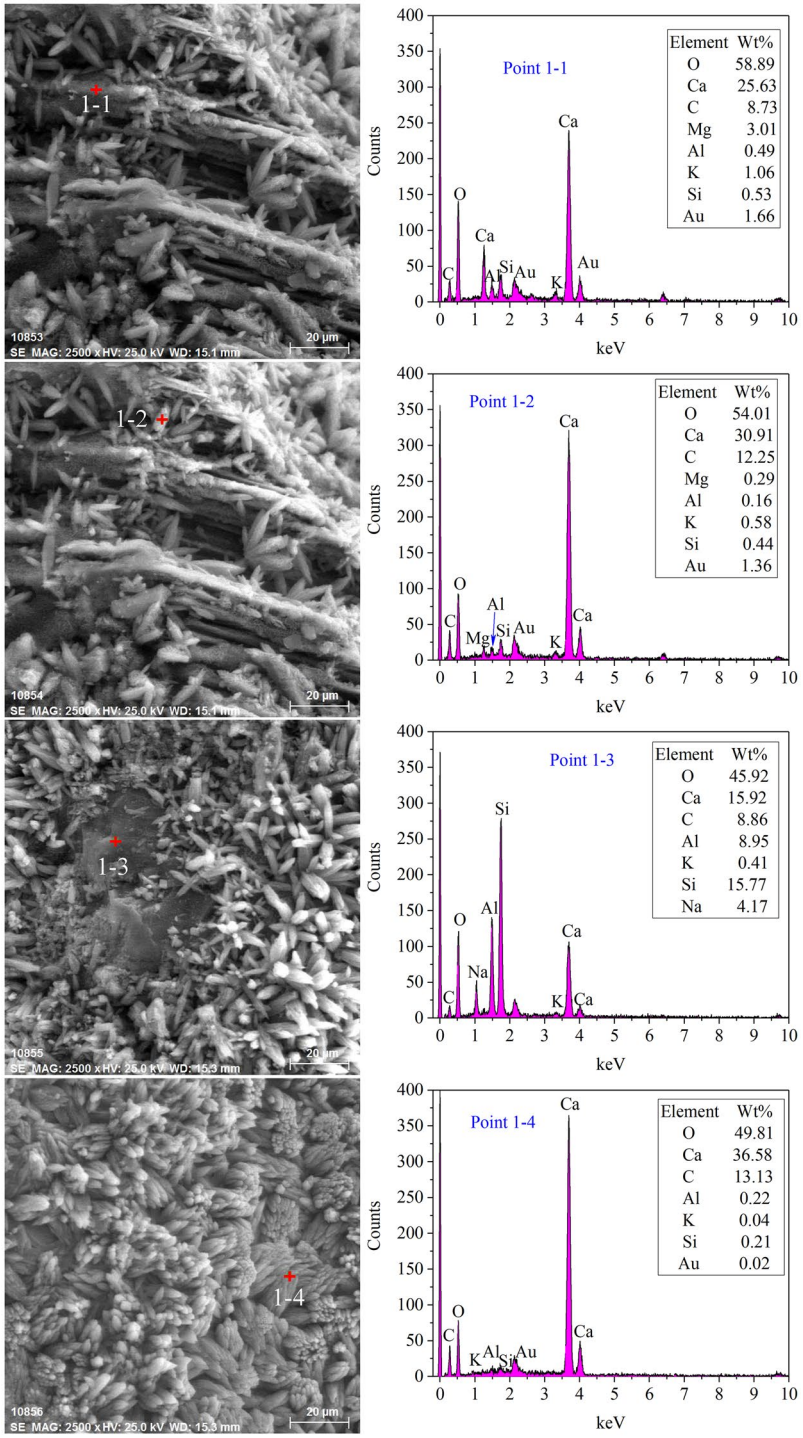

Fig. 8 SEM–EDS analysis results of the mineral components in area 1

At point 2–2, without considering the minor and trace elements, the atomic number ratio of each element was calculated to be O:Ca:C:Si = 12:2:6.38:1. Therefore, the mineral particles at this point are mainly calcite, and there is a quartz mineral base nearby. The minerals and elements at points 2–3 and 2–2 were found to be consistent

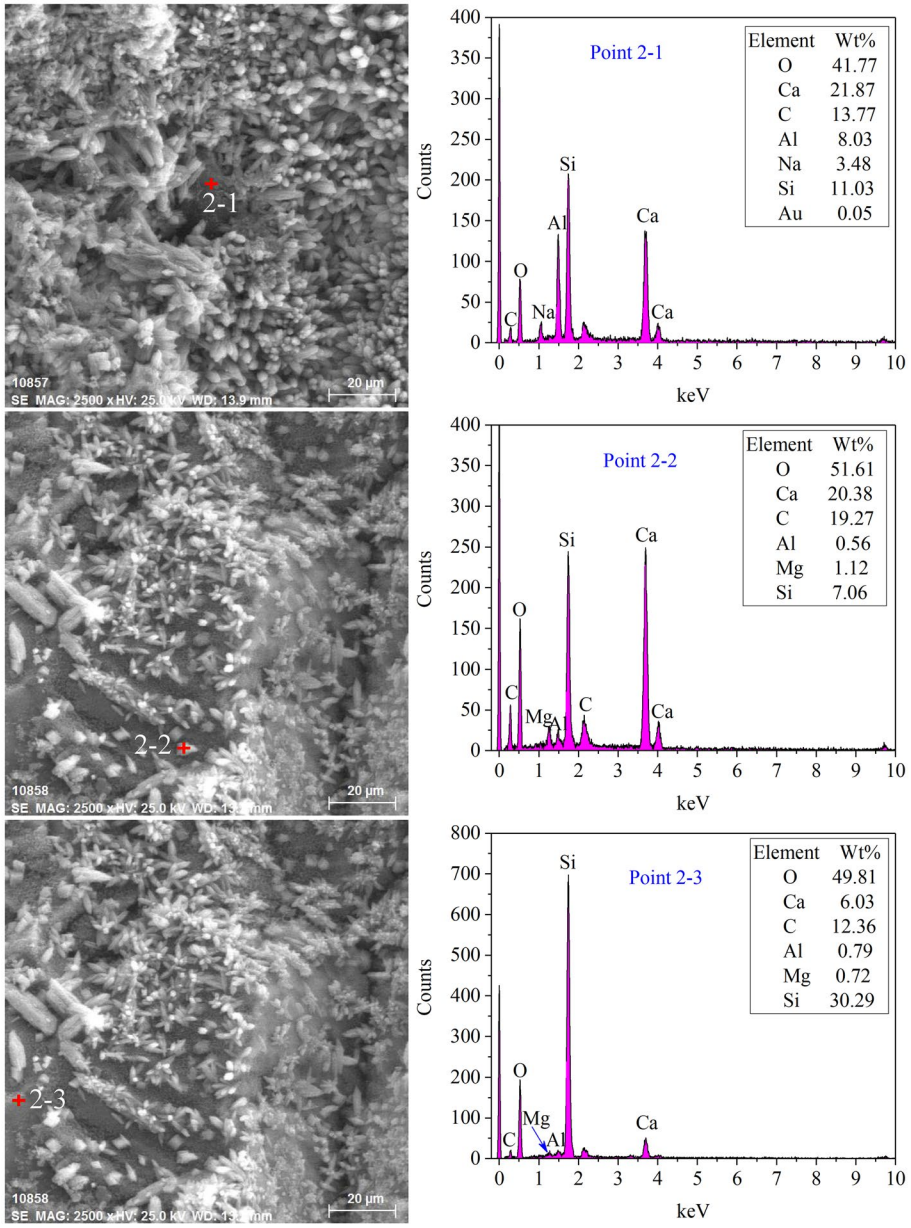

Fig. 9 SEM–EDS analysis results of mineral components in area 2

in type, but the content of Si increases and the content of Ca decreases at point 2–3. Therefore, the mineral at point 2–3 is the primary quartz on the fracture surface with a small amount of calcite crystals attached to it.

Figure 10 shows the SEM–EDS analysis results of the mineral components in area 3. It can be seen from the morphology that the mineral at point 3–1 is the mineral base of the fracture surface. The analysis of the mineral's composition shows that the Al and Si contents are relatively high, so it was concluded to be aluminosilicate. In addition, it also contains K, Fe, and Mg, which indicates that it is biotite.

At point 3–2, the element contents reveal that the O and Ca contents are high, but there is no C present. The ratio of the atomic number of each element calculated has no

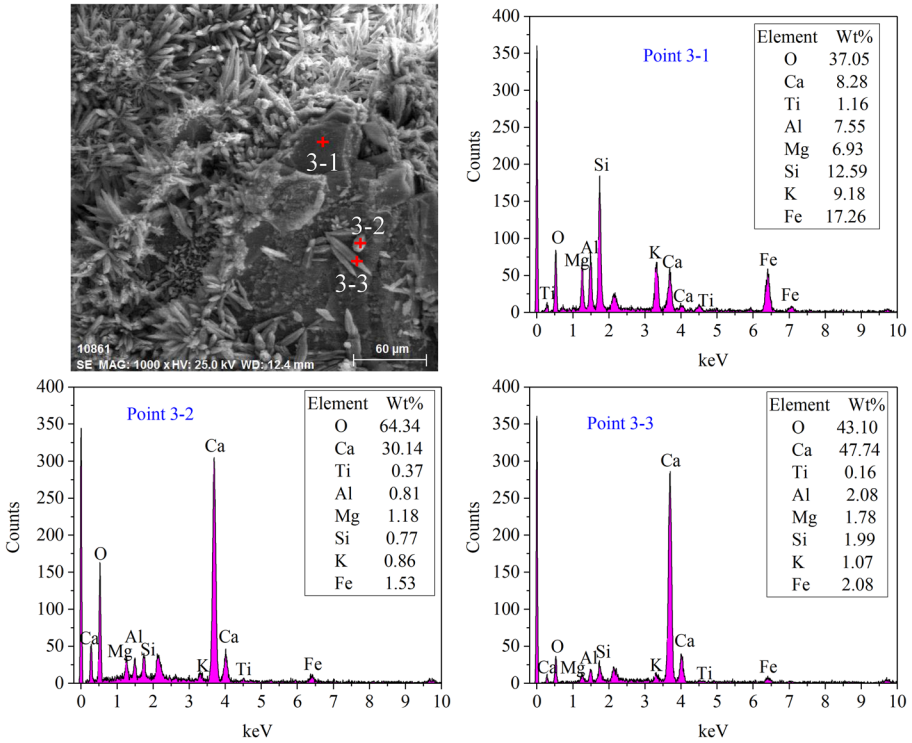

Fig. 10 SEM–EDS analysis results of mineral components in area 3

specific rule, and the minerals occur as irregular granules. Therefore, it is inferred that the minerals are Ca, Al, Mg, K, and Fe oxides, with a high CaO content. The types of elements in the mineral at point 3–3 are the same as those at point 3–2, but the Ca content is slightly lower, while the Al and Si contents are higher. Moreover, the mineral is needle like, so it was concluded that the aluminosilicate at this point is scolecite.

According to the above SEM–EDS results, the influence of the new minerals on the morphology of the primary mineral base of the fracture surface after the experiment can be analyzed. Figure 11 shows the SEM images of the fracture surface of rock sample CA-2 before and after the experiment. Before the experiment (Fig. 11a–c), the morphology of the primary minerals on the surface of the main fracture is relatively flat, and that of the minerals in the microfractures and micropores is clear and smooth. After the experiment, highly crystalline granules and rod-like calcite were observed near the microfractures (Fig. 11d and e). In the microfractures and micropores (Fig. 11f), highly crystalline rod-like clusters of calcite and hairball squama of montmorillonite were formed. Furthermore, highly crystalline rod-like calcite crystal clusters (Fig. 11g and h) and blocky carbonates such as $CaCO_3$ and $CaMg(CO_3)_2$ (dolomite) were formed on the main fracture surface and between the narrow minerals (Fig. 11i).

It can be seen that the CO_2-water–rock interactions in the fracture resulted in obvious mineral dissolution and precipitation. At the same time, the types and morphology of mineral crystallization on the surface of main fracture, micro-fractures and micropores were different. There are two main reasons for this result. On the surface of the main fracture, the difference of CO_2 velocity caused by concave-convex mineral particles

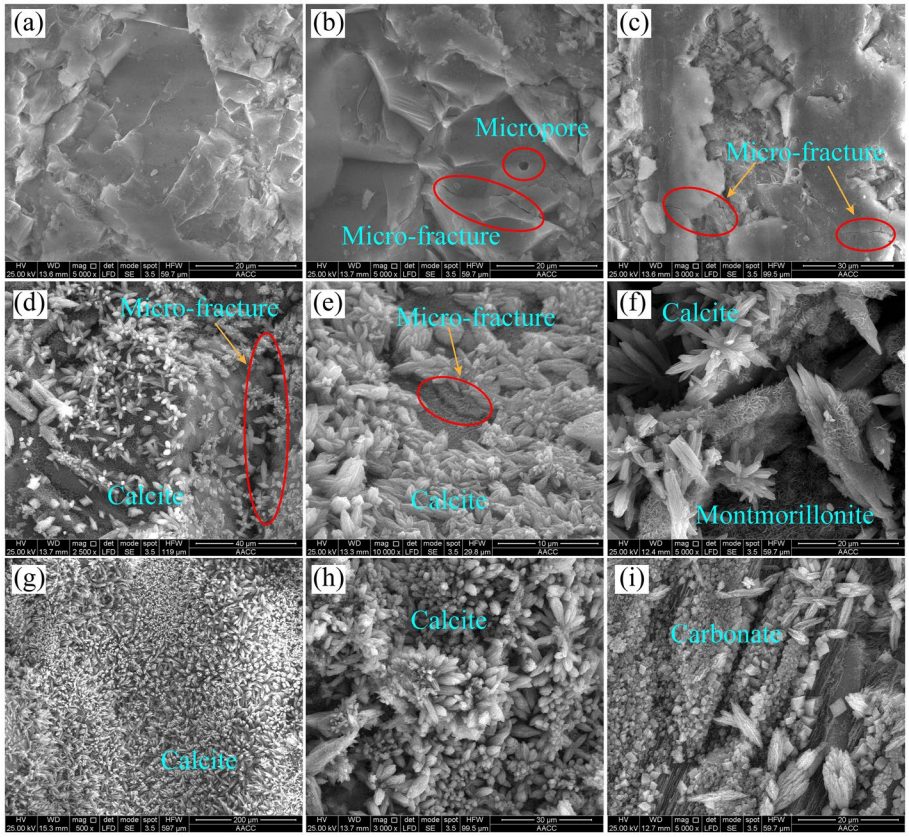

Fig. 11 SEM images of the fracture surface in rock sample CA-2 (**a**–**c**) before and (**d**–**i**) after the experiment

changes the CO_2-water–rock interaction time. While for the surface of unconnected micro-fractures or micropores, the difference in mineral crystallization is mainly caused by residual trapping effect (Wu and Li 2020). This mineral crystallization changes the roughness of the fracture surface, affects the flow of CO_2, and has a significant impact on the permeability (Huang et al. 2019; Wang et al. 2016; Fang et al. 2018). Therefore, we further analyzed the coupled thermo-hydro-mechanical–chemical effect on the evolution of the fracture permeability.

Permeability evolution in the absence and presence of proppant

In the absence of proppant, the permeability evolution of rock sample CA-1 with increasing number of injection cycles is shown in Fig. 12. It can be seen that the overall permeability decreased as the number of injection cycles increased, but the reduction rate of the permeability varied greatly in the different stages.

It can be seen that during injection cycles 0–1, the permeability decreased at the highest rate and within the largest range. This stage was mainly affected by pressure dissolution (Lu et al. 2018; Yasuhara et al. 2004). On the surfaces of the fracture, some convex particles had asperity contact under the action of the pressure (see Fig. 13a). The contact part of the particles was squeezed and a large number of microfractures formed, which resulted in a crushed zone (see Fig. 13b). In this zone, the mineral dissolution was enhanced. The crushed particulate solute slowly diffused into the main

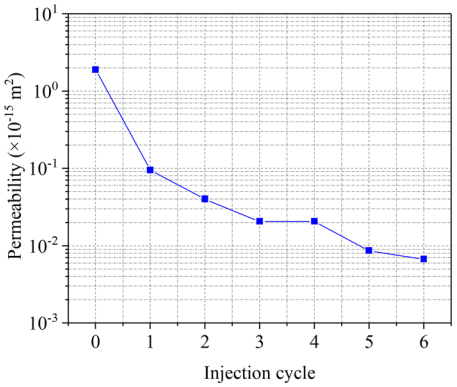

Fig. 12 Permeability evolution of rock sample CA-1 with increasing number of injection cycles

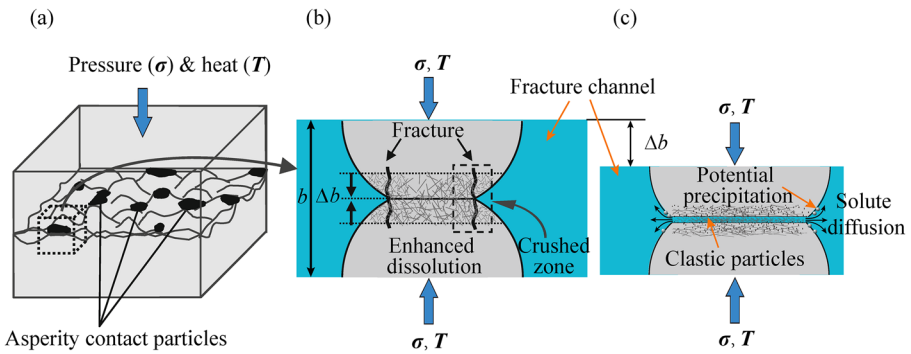

Fig. 13 Schematic diagram of the pressure dissolution effect on the asperity contact particles of the fracture surface. **a** convex particles contact, **b** crushed zone is formed by squeezing, **c** mineral dissolution and precipitation (adopted from Yasuhara et al. 2004)

fracture channel and generated mineral precipitation near the particles (see Fig. 13c). As the pressure dissolution continued, the contact area between the particles gradually increased, and the effect of the pressure dissolution gradually weakened. Therefore, the average hydraulic aperture b of the fracture decreased to $b - \Delta b$, where Δb is the average width of the pressure dissolution zone. It can be seen that the coupled thermo (T)-hydro-mechanical (σ)–chemical effect affected the hydraulic aperture during this process. The variations in the hydraulic aperture before and after the pressure dissolution are shown in Fig. 14.

During injection cycles 1–3 and 4–6, the reduction rate of the permeability tended to decrease to different degrees. During the injection cycle 6, the pressure dissolution caused weakening and disintegration of the particle contact positions, resulting in three distinct stages of permeability variation. In the first stage (i.e., injection cycles 0–1), the dissolutions of albite, anorthite and potassium feldspar mainly occurred at the particle contact positions on the fracture surface, and the potential precipitations of calcite, dolomite, kaolinite and illite were generated on the fracture's free surface. In the two subsequent stages (i.e., injection cycles 1–3 and 4–6), the mineral dissolution and precipitation on the free surface gradually became apparent. The significant mineral precipitation reduced the fracture aperture, which led to a decrease in

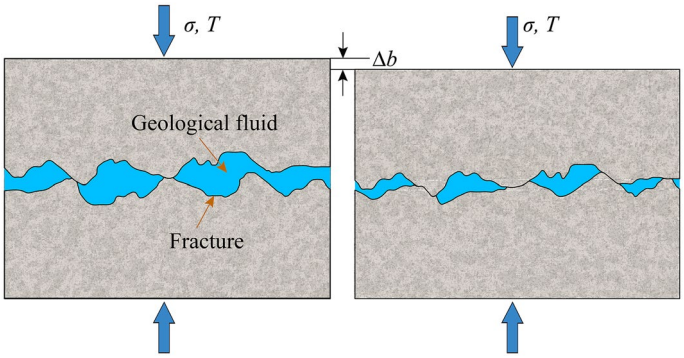

Fig. 14 Schematic diagram of the variations in the hydraulic aperture in the absence of proppant before (left) and after (right) pressure dissolution (adopted from Yasuhara et al. 2004)

the permeability. Owing to the non-isothermal flow of the water and CO_2, the matrix heat conduction affected the CO_2 dissolution and the other chemical processes near the fracture's free surface, thus affecting the permeability.

The permeability evolution of rock sample CA-2 with increasing number of injection cycles is shown in Fig. 15. Compared with rock sample CA-1, when the two rock samples had a similar initial permeability, their permeabilities after the experiment were also relatively close. Moreover, there were also three stages of permeability evolution. In the first stage (i.e., injection cycles 0–1), the pressure dissolution had an intense effect on the permeability. The difference is that in the two subsequent stages (i.e., injection cycles 1–5 and 5–9), the reduction rate of the permeability was relatively slow at the beginning of each stage, but it gradually increased as the number of injection cycles increased. In general, the reduction rate of the permeability exhibited a sharp-slow–fast–slow trend. These results indicate that the contact particles on the fracture's surface underwent strength weakening stage (expansion of the crushed zone), a dissolution and disintegration stage, and a stabilization stage (i.e., re-contact of mineral particles) under the THMC effect.

Figure 16 is a schematic diagram of the variations in the hydraulic fracture aperture in the presence of a proppant before and after pressure dissolution. The contact form of the fracture surface changed from particle–particle contact to

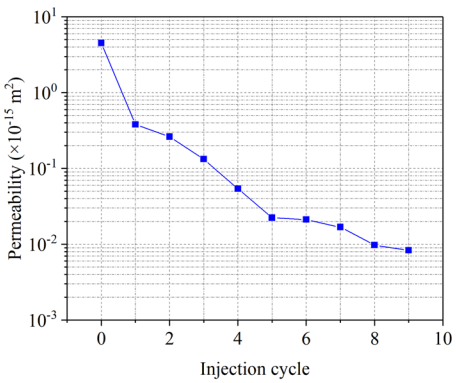

Fig. 15 Permeability evolution of rock sample CA-2 with increasing number of injection cycles

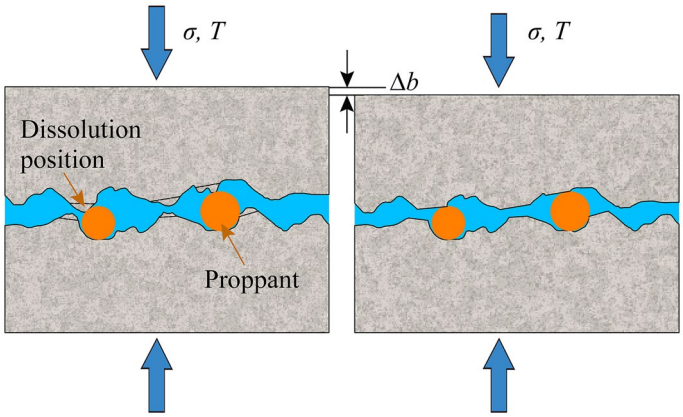

Fig. 16 Schematic diagram of the variations in the hydraulic fracture aperture in the presence of a proppant before (left) and after (right) pressure dissolution

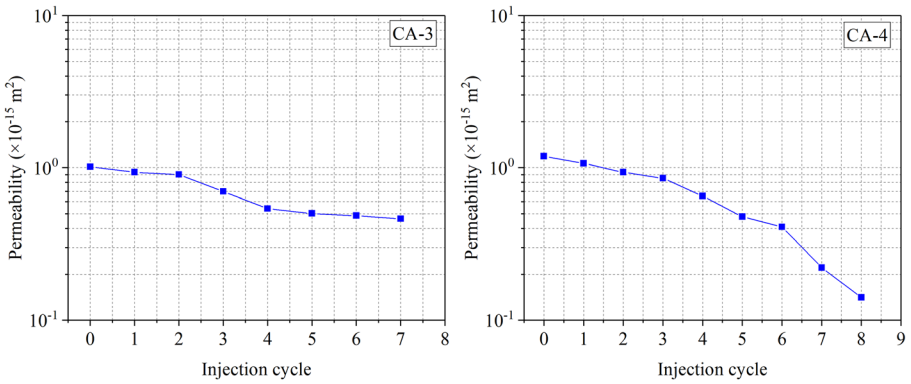

Fig. 17 Permeability evolution of rock samples CA-3 and CA-4 with increasing number of injection cycles

particle-proppant-particle, particle-proppant-free surface, and free surface-proppant-free surface contacts.

When the pressure did not exceed the proppant's failure strength (about 52 MPa), the first two contact forms were more likely to cause pressure dissolution at the proppant-particle contact positions, resulting in a small reduction in the fracture aperture. For the third contact form, the pressure dissolution on the free surface was not obvious because the granite's strength was slightly higher than that of the proppant. Under certain conditions, the pressure may be higher than the failure strength of the proppant. At this time, the proppant is gradually damaged, resulting in a significant reduction of the fracture aperture and thus a decrease in the permeability.

In the presence of a proppant, the permeability evolutions of rock samples CA-3 and CA-4 with increasing number of injection cycles are shown in Fig. 17. It can be seen that the permeabilities of the two samples still decreased. However, there was no order of magnitude change in the decrease in the permeability. Therefore, the ability to maintain the high permeability of the reservoir is significantly better than that without proppant. Moreover, the permeability had a relatively small reduction rate during injection

cycles 0–2 for rock sample CA-3 and during injection cycles 0–3 for rock sample CA-4. Therefore, during the initial injection cycle stage, the addition of proppant reduced the asperity contact portions on the fracture surface, which in turn significantly reduced the pressure dissolution effect. However, as the number of injection cycles increased (injection cycles 2–4 for CA-3 and injection cycles 3–5 for CA-4), the convex particles in contact with the proppant on the fracture surface disintegrated under the pressure, resulting in a small decrease in the fracture aperture and a relatively significant decrease in the permeability.

During the subsequent injection cycles, the reduction rate of the permeability of rock sample CA-3 gradually tended to zero, while that of rock sample CA-4 initially decreased in injection cycles 5–6, and then increased significantly in injection cycles 6–8. These results show that the particle-proppant-free surface contact form dominated the fractures in rock sample CA-3, while the particle-proppant-particle contact form was dominant in rock sample CA-4. In addition, it was also found that neither condition (with and without proppant) resulted in a significant decrease in the permeability when the pressure dissolution of the fracture surface stabilized.

Conclusions

In a CO_2-EGS reservoir, CO_2 (sc) injection results in CO_2-water–rock interactions and generates the mineralization storage of CO_2. The coupled THMC effect during this process has a great influence on the permeability. In this study, CO_2 storage and heat extraction were simulated by alternating cyclic injection of water and supercritical CO_2 into fractured granite. The influence of the coupled THMC effect on reservoir permeability was studied, and the mechanism of the above effect on the reservoir permeability with and without proppant was analyzed. The following conclusions were obtained:

(1) As the number of injection cycles increased, the minerals dissolved on the fracture surface in the granite were still mainly feldspars including albite, anorthite, and potassium feldspar. As the Na^+ and K^+ contents increased, a small amount of biotite was also dissolved. However, in addition to cancrinite, dolomite, kaolinite, montmorillonite, calcite and illite, the newly formed minerals included monticellite and vaterite (a thermally unstable phase of $CaCO_3$) as well after increasing the number of injection cycles. It promotes mineralization storage of CO_2 but reduces reservoir permeability. This indicates that the duration of the CO_2-water–rock interactions had a significant influence on the form of the mineral dissolution and precipitation. Therefore, selecting a reasonable CO_2 (sc) injection pressure and injection flow rate can shorten the above process and reduce the influence on the fracture's permeability.

(2) After the dissolution of the primary mineral base, owing to the difference in the CO_2 flow velocity and the effect of the residual trapping in the micropores/microfractures, the type of mineral precipitation varied with the positions of the fracture surface. Highly crystalline rod-like calcite and hairball squama montmorillonite were formed in the relatively clear and smooth microfractures and micropores, while highly crystalline granular or rod-like calcite crystal clusters were formed near the microfractures. Also, on the main fracture surface and between the nar-

row minerals, highly crystalline rod-like calcite crystal clusters and other blocky carbonate mineral crystallization were formed. These carbonate crystallizations formed by mineralization storage of CO_2 significantly affect porosity and permeability of fractured granite.

(3) In the absence of the proppant, the pressure dissolution had a significant impact on the fracture surfaces in the initial stage, and the permeability decreased sharply. As the number of the injection cycles increased, the asperity contact particles on the fracture surfaces were dissolved and disintegrated continuously, which caused the reduction rate of the permeability to exhibit a sharp-slow–fast–slow trend. While in the presence of the proppant, the contact form on the fracture surfaces was changed, which decreased the effect of the initial pressure dissolution. In the middle stage, the mineral particles on the fracture surfaces in contact with the proppant dissolved under the pressure, leading to a small decrease in the permeability. However, compared to the condition without proppant, the use of proppant caused an increase of approximately two orders of magnitude in permeability. Therefore, increasing the non-contact area of the main fracture can avoid a large decrease in permeability, which will increase the heat extraction and mineralization storage of CO_2.

Abbreviations

HDR	Hot dry rock
CO_2-EGS	CO_2-based enhanced geothermal system
THMC	Thermo-Hydro-Mechanical-Chemical
XRD	X-ray diffraction
EDS	Energy dispersive spectroscopy
SEM	Scanning electron microscopy

List of symbols

v_f	The average flow velocity of CO_2, m/s
w	The average fracture aperture, mm
ρ_f	The density of the CO_2, kg/m^3
μ	The dynamic viscosity of the CO_2, Pa·s
k	The permeability, m^2
b	The equivalent hydraulic aperture, mm
g	The acceleration due to gravity, m/s^2
p_{in}	The pressure of the CO_2 at the inlet, Pa
p_{out}	The pressure of the CO_2 at the outlet, Pa
L	The length of the rock sample, mm
Q_f	The volume flow rate of the CO_2, m^3/s
T	The temperature of reservoir, °C
σ	The stress of reservoir, Pa

Fluid phase state

sc	Supercritical state

Acknowledgements

We thank LetPub (www.letpub.com) for its linguistic assistance during the preparation of this manuscript. We also thank anonymous reviewers and the Prof. Shao for their professional guidance and assistance on our manuscript.

Author contributions

PL measured and analyzed the data, prepared the figures, and wrote the first draft of the manuscript. YH conducted the sampling, sample preparation. YW helped in designing the study, contributed to the writing and the discussion of the results. AW substantially contributed by revising and structuring this work. HXZ conducted permeability test and analysis, helped improve the quality of this work. ZLC conducted some of the petrophysical measurements and microstructural investigations. All the authors read and approved the final manuscript.

Funding

This work was supported by Scientific Research Foundation for High-level Talents of Anhui University of Science and Technology [Grant number 13200394]; State Key Laboratory for Geomechanics and Deep Underground Engineering,

China University of Mining and Technology [Grant number SKLGDUEK2112]; Anhui University Natural Science Foundation [Grant number KJ2020A0329].

Availability of data and materials
All data generated or analyzed during this study are included in this published article.

Declarations

Competing interests
The authors have no competing interest to declare.

Received: 13 January 2023 Accepted: 2 August 2023
Published online: 09 August 2023

References

Ager JW, Lapkin AA. Energy storage chemical storage of renewable energy. Science. 2018;360:707–8. https://doi.org/10.1126/science.aat7918.
Caulk RA, Ghazanfari E, Perdrial JN, Perdrial N. Experimental investigation of fracture aperture and permeability change within enhanced geothermal systems. Geothermics. 2016;62:12–21. https://doi.org/10.1016/j.geothermics.2016.02.003.
Dempsey D, Kelkar S, Davatzes N, Hickman S, Moos D. Numerical modeling of injection, stress and permeability enhancement during shear stimulation at the desert peak enhanced geothermal system. Int J Rock Mech Min. 2015;78:190–206. https://doi.org/10.1016/j.ijrmms.2015.06.003.
Deng M, Zhong S, Xiang G. Carbon emission reduction effect of China's final demand structure change from 2013 to 2020: a scenario-based analysis. Carbon Manag. 2019;10:387–404. https://doi.org/10.1080/17583004.2019.1620036.
Fang Y, Elsworth D, Ishibashi T, Zhang F. Permeability evolution and frictional stability of fabricated fractures with specified roughness. J Geophys Res Solid Earth. 2018;123:9355–75. https://doi.org/10.1029/2018JB016215.
Frank S, Havlik P, Stehfest E, van Meijl H, Witzke P, Perez-Dominguez I, van Dijk M, Doelman JC, Fellmann T, Koopman JFL, Tabeau A, Valin H. Agricultural non-CO2 emission reduction potential in the context of the 1.5 degrees C target. Nat Clim Change. 2019;9:66–72. https://doi.org/10.1038/s41558-018-0358-8.
Guo X, Zou GF, Wang YH, Wang Y, Gao T. Investigation of the temperature effect on rock permeability sensitivity. J Petrol Sci Eng. 2017;156:616–22. https://doi.org/10.1016/j.petrol.2017.06.045.
Guo S, Yan D, Hong T, Xiao C, Cui Y. A novel approach for selecting typical hot-year (THY) weather data. Appl Energy. 2019;242:1634–48. https://doi.org/10.1016/j.apenergy.2019.03.065.
Hou J, Cao M, Liu P. Development and utilization of geothermal energy in China: current practices and future strategies. Renew Energy. 2018;125:401–12. https://doi.org/10.1016/j.renene.2018.02.115.
Huang Y, Zhang Y, Yu Z, Ma Y, Zhang C. Experimental investigation of seepage and heat transfer in rough fractures for enhanced geothermal systems. Renew Energy. 2019;135:846–55. https://doi.org/10.1016/j.renene.2018.12.063.
Huang Y, Zhang Y, Gao X, Ma Y, Hu Z. Experimental and numerical investigation of seepage and heat transfer in rough single fracture for thermal reservoir. Geothermics. 2021;95:102163. https://doi.org/10.1016/j.geothermics.2021.102163.
IEA. Renewables. 2021. https://www.iea.org/fuels-and-technologies/renewables. Accessed 15 May 2022.
Kamali-Asl A, Ghazanfari E, Perdrial N, Bredice N. Experimental study of fracture response in granite specimens subjected to hydrothermal conditions relevant for enhanced geothermal systems. Geothermics. 2018;72:205–24. https://doi.org/10.1016/j.geothermics.2017.11.014.
Kaya E, Callos V, Mannington W. CO_2–water mixture reinjection into two-phase liquid dominated geothermal reservoirs. Renew Energy. 2018;126:652–67. https://doi.org/10.1016/j.renene.2018.03.067.
Kolditz O. Non-linear flow in fractured rock. Int J Numer Method h. 2001;11:547–75. https://doi.org/10.1108/EUM0000000005668.
Ledésert B, Hebert R, Genter A, Bartier D, Clauer N, Grall C. Fractures, hydrothermal alterations and permeability in the Soultz enhanced geothermal system. Cr Geosci. 2010;342:607–15. https://doi.org/10.1016/j.crte.2009.09.011.
Li B, Haneklaus N. The role of renewable energy, fossil fuel consumption, urbanization and economic growth on CO_2 emissions in China. Energy Rep. 2021;7:783–91. https://doi.org/10.1016/j.egyr.2021.09.194.
Liao J, Hou Z, Haris M, Tao Y, Xie Y, Yue Y. Numerical evaluation of hot dry rock reservoir through stimulation and heat extraction using a three-dimensional anisotropic coupled THM model. Geothermics. 2020;83:101729. https://doi.org/10.1016/j.geothermics.2019.101729.
Liu L, Suto Y, Bignall G, Yamasaki N, Hashida T. CO_2 injection to granite and sandstone in experimental rock/hot water systems. Energy Convers Manage. 2003;44:1399–410. https://doi.org/10.1016/S0196-8904(02)00160-7.
Liu J, Wang Z, Shi W, Tan X. Experiments on the thermally enhanced permeability of tight rocks: a potential thermal stimulation method for enhanced geothermal systems. Energy Sources Part A Recovery Util Environ Effects. 2020. https://doi.org/10.1080/15567036.2020.1745332.
Lu R, Nagel T, Shao H, Kolditz O, Shao H. Modeling of dissolution-induced permeability evolution of a granite fracture under crustal conditions. J Geophys Res Solid Earth. 2018;123:5609–27. https://doi.org/10.1029/2018JB015702.
Meinshausen M, Lewis J, McGlade C, Gütschow J, Nicholls Z, Burdon R, Cozzi L, Hackmann B. Realization of Paris agreement pledges may limit warming just below 2 °C. Nature. 2022;604:304–9. https://doi.org/10.1038/s41586-022-04553-z.
Na J, Xu TF, Yuan YL, Feng B, Tian HL, Bao XH. An integrated study of fluid-rock interaction in a CO_2-based enhanced geothermal system: a case study of Songliao Basin. China Appl Geochem. 2015;59:166–77. https://doi.org/10.1016/j.apgeochem.2015.04.018.

Pruess K. Enhanced geothermal systems (EGS) using CO_2 as working fluid—a novel approach for generating renewable energy with simultaneous sequestration of carbon. Geothermics. 2006;35:351–67. https://doi.org/10.1016/j.geothermics.2006.08.002.
Ranjith PG, Viete DR. Applicability of the 'cubic law' for non-Darcian fracture flow. J Pet Sci Eng. 2011;78:321–7. https://doi.org/10.1016/j.petrol.2011.07.015.
Ré CL, Kaszuba JP, Moore JN, McPherson BJ. Fluid-rock interactions in CO_2-saturated, granite-hosted geothermal systems: Implications for natural and engineered systems from geochemical experiments and models. Geochim Cosmochim Ac. 2014;141:160–78. https://doi.org/10.1016/j.gca.2014.06.015.
Sawayama K, Ishibashi T, Jiang F, Tsuji T, Nishizawa O, Fujimitsu Y. Scale-independent relationship between permeability and resistivity in mated fractures with natural rough surfaces. Geothermics. 2021;94:102065. https://doi.org/10.1016/j.geothermics.2021.102065.
Shams G, Rivard P, Moradian O. Observation of fracture process zone and produced fracture surface roughness in granite under Brazilian splitting tests. Theor Appl Fracture Mech. 2023;125:103680. https://doi.org/10.1016/j.tafmec.2022.103680.
Shu B, Zhu R, Elsworth D, Dick J, Liu S, Tan J, Zhang S. Effect of temperature and confining pressure on the evolution of hydraulic and heat transfer properties of geothermal fracture in granite. Appl Energy. 2020;272:115290. https://doi.org/10.1016/j.apenergy.2020.115290.
Song C, Nakashima S, Kido R, Yasuhara H, Kishida K. Short- and long-term observations of fracture permeability in granite by flow-through tests and comparative observation by X-Ray CT. Int J Geomech. 2021;21:04021151. https://doi.org/10.1061/%28ASCE%29GM.1943-5622.0002114.
Subramanian T, Geo VE, Martin LJ, Nagalingam B. Mitigation of carbon footprints through a blend of biofuels and oxygenates, combined with post-combustion capture system in a single cylinder CI engine. Renew Energy. 2019;130:1067–81. https://doi.org/10.1016/j.renene.2018.07.010.
Tao J, Wu Y, Elsworth D, Li P, Hao Y. Coupled thermo-hydro-mechanical-chemical modeling of permeability evolution in a CO_2-circulated geothermal reservoir. Geofluids. 2019. https://doi.org/10.1155/2019/5210730.
Ueda A, Kato K, Ohsumi T, Yajima T, Ito H, Kaieda H, Metcalfe R, Takase H. Experimental studies of CO_2-rock interaction at elevated temperatures under hydrothermal conditions. Geochem J. 2005;39:417–25. https://doi.org/10.2343/geochemj.39.417.
Wang M, Chen Y-F, Ma G-W, Zhou J-Q, Zhou C-B. Influence of surface roughness on nonlinear flow behaviors in 3D self-affine rough fractures: lattice Boltzmann simulations. Adv Water Resour. 2016;96:373–88. https://doi.org/10.1016/j.advwatres.2016.08.006.
Wu Y, Li P. The potential of coupled carbon storage and geothermal extraction in a CO_2-enhanced geothermal system: a review. Geotherm Energy. 2020;8:19. https://doi.org/10.1186/s40517-020-00173-w.
Wu Y, Li P, Hao Y, Wanniarachchi A, Zhang Y, Peng S. Experimental research on carbon storage in a CO_2-based enhanced geothermal system. Renew Energy. 2021;175:68–79. https://doi.org/10.1016/j.renene.2021.04.139.
Yasuhara H, Elsworth D, Polak A. Evolution of permeability in a natural fracture: significant role of pressure solution. J Geophys Res-Sol Ea. 2004. https://doi.org/10.1029/2003JB002663.

Publisher's Note